Chinese Chemical Letters 36 (2025) 110341

Contents lists available at ScienceDirect

Chinese Chemical Letters

journal homepage: www.elsevier.com/locate/cclet

Design of near-infrared aggregation-induced emission photosensitizers by π-bridge engineering for boosting theranostic efficacy

Tong-Tong Zhou[a,1], Guan-Yu Ding[a,d,1], Xue Li[a,1], Li-Li Wen[a,*], Xiao-Xu Pang[a], Ying-Chen Duan[a,*], Ju-Yang He[c], Guo-Gang Shan[b,*], Zhong-Min Su[a,*]

[a] School of Chemistry and Environmental Engineering and Jilin Provincial Science and Technology Innovation Center of Optical Materials and Chemistry, Changchun University of Science and Technology, Changchun 130022, China
[b] National & Local United Engineering Laboratory for Power Batteries, Department of Chemistry, Northeast Normal University, Changchun 130024, China
[c] Department of Gynecological Oncology, The First Hospital of Jilin University, Changchun 130012, China
[d] State Key Laboratory of Electroanalytical Chemistry, Changchun Institute of Applied Chemistry, Chinese Academy of Sciences (CAS), Changchun 130022, China

ARTICLE INFO

Article history:
Received 8 July 2024
Revised 12 August 2024
Accepted 13 August 2024
Available online 14 August 2024

Keywords:
Fluorescence imaging-guided photodynamic therapy
Photosensitizers
Aggregation-induced emission
π-bridge modulation
Type I and II ROS generation
Antitumor efficacy

ABSTRACT

Fluorescence imaging-guided photodynamic therapy holds great promise for application in precise cancer diagnosis and treatment, which has motivated high requirements for phototheranostic agents. However, current photosensitizers (PSs) generally face limitations such as short emission wavelength and inadequate reactive oxygen species (ROS) production. Aggregation-caused quenching issue also hinders the phototheranostic efficiency of PSs. Herein, the π-bridge modulation strategy is proposed to construct ionic PSs with enhanced bioimaging and therapeutic outcomes. Two donor-π-acceptor (D-π-A) molecules **TPCPY** and **TFCPY** were obtained by incorporating phenyl and furan units as π-bridge, respectively. Both PSs feature aggregation-induced near-infrared emission. Under light irradiation, **TPCPY** and **TFCPY** can produce both type I and II ROS. Introducing furan ring in **TFCPY** enhances the ROS generation capacity by type I photosensitization process, which is consistent with the reduced energy gap between singlet and triplet states from theoretical calculation. Furthermore, **TFCPY** can achieve quick cellular uptake, accumulate in mitochondria, and then efficiently kill cancer cells, which is superior to **TPCPY**. Consequently, **TFCPY** exhibited good antitumor outcomes and excellent *in vivo* fluorescence imaging ability. This work provides an efficient molecular engineering of introducing heterocycles into the D-π-A skeleton to develop high-performance PSs with both type I and II ROS generation.

As the main health burden for humankind worldwide, cancer has caused almost tens of thousands of deaths every year [1,2]. The development of efficient diagnosis and treatment modalities against cancer has become increasingly urgent and essential. As a clinically approved protocol for cancer phototheranostics, fluorescence imaging-guided photodynamic therapy (FLI-guided PDT) has garnered considerable interest because of its distinct advantages, including non-invasiveness, controllability, and negligible drug resistance [3-5]. Viewed in FLI-guided PDT, the photosensitizers (PSs) can generate cytotoxic reactive oxygen (ROS) upon exposure to light irradiation, which can eradicate tumor cells [6-9]. In addition, the emission ability of designed PSs can enable FLI, achieving real-time monitoring of tumor tissue. Generally, concerted efforts have been devoted to designing PSs with strong light absorption, high emission efficiency, and high ROS sensitization capacity for FLI-guided PDT. In PDT, the PSs can undergo type I or type II photochemical reactions to produce toxic radicals (superoxide anion $O_2^{\bullet-}$, hydroxyl radical $^{\bullet}OH$, *etc.*) or singlet oxygen ($^1O_2$), respectively [10]. Type II PDT depends on oxygen concentration in the surrounding microenvironment, which compromises the therapeutic efficacy in hypoxic solid tumors [11]. Different from type II PDT, type I PDT shows more promise for deactivating the solid tumors owing to the oxygen-less-dependent path [12-15]. However, classical PSs work through type II photosensitization because of the much faster process of type II than type I. Constructing advanced PSs capable of generating type I/II ROS is an effective approach for enhancing PDT efficacy and eliminating tumors [16,17].

Organic PSs have been investigated and applied in FLI-guided PDT broadly owing to low toxicity, well-definite composition, good

* Corresponding authors.
E-mail addresses: wll@cust.edu.cn (L.-L. Wen), duanyc122@nenu.edu.cn (Y.-C. Duan), shangg187@nenu.edu.cn (G.-G. Shan), zmsu@nenu.edu.cn (Z.-M. Su).
[1] These authors contributed equally to this work.

https://doi.org/10.1016/j.cclet.2024.110341
1001-8417/

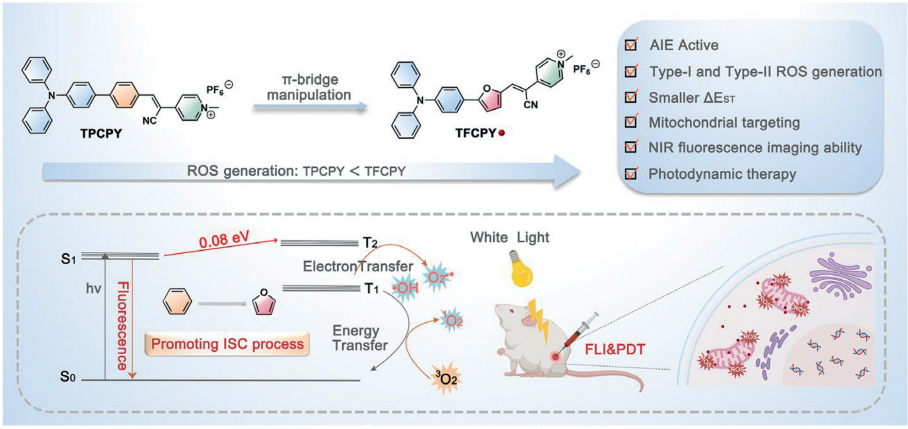

Scheme 1. Schematic illustration of π bridge engineering of **TPCPY** and **TFCPY**, and FLI-guided PDT.

biocompatibility, and facile molecular tailoring [18,19]. However, the conventional organic PSs with the planar hydrophobic molecular skeleton tend to aggregate in biological environments, leading to a drastic decrease in both emission efficiency and photosensitivity [20]. To address these challenges, the construction of PSs with aggregation-induced emission (AIE) nature emerges as a promising strategy [21-25]. AIE-active PSs exhibit brighter emission and enhanced ROS generation in the aggregate state [26-28]. Considering the advantages of near-infrared (NIR) light such as deep penetration and reduced interference with tissue photodamage, the concise development of AIE-active PSs with NIR emission holds tremendous promise for boosting FLI-guided PDT efficiency [29-32]. Generally, donor-π-acceptor (D-π-A) molecular engineering has been widely employed to construct AIE PSs [33,34]. This molecular design strategy is beneficial for narrowing singlet-triplet energy gaps, thus enhancing the intersystem crossing (ISC) process and achieving efficient ROS production [35,36]. Despite significant progress has been made in developing AIE PSs for FLI-guided PDT application, there is a deficiency in constructing AIE-based PSs capable of efficient NIR fluorescence and excellent type I/II ROS generation. The new design strategy and clear structure-property is also desired.

To achieve good anticancer performance, in this work, two appealing PSs named **TPCPY** and **TFCPY** were designed and synthesized by the integration of electron-withdrawing and electron-donating units on different π bridges, as shown in Scheme 1. The impact of π bridges in the D-π-A molecular skeleton on curative effect was investigated systematically. Selecting an electron-rich furan group as π-bridge rather than a phenyl unit enables **TFCPY** with red-shifted absorption, enhanced molar absorption coefficient, and NIR emission. Both compounds were demonstrated to possess superior ROS generation ability than commercially available Rose Bengal (RB) as well as chlorin e6 (Ce6). Moreover, **TPCPY** and **TFCPY** can produce $^1O_2$, $O_2^{\bullet-}$, and $^{\bullet}OH$ simultaneously, displaying type I/II combined PDT capability. **TFCPY** with furan π-bridge exhibited relatively higher type I ROS compared with that of **TPCPY**, which can be attributed to a smaller energy gap (0.08 eV) between first singlet excited state (S_1) and 2nd triplet excited states (T_2). Subsequently, intracellular experiments demonstrated that **TFCPY** performed superior cellular imaging, ROS generation capability, and prominent anti-cancer cell ability contrasted with **TPCPY**. Furthermore, *in vivo* PDT results reveal that **TFCPY** effectively achieves fluorescence imaging and inhibits tumor growth.

To systematically study the effect of π-conjugation bridge engineering in regulating the photoluminescence (PL) properties and ROS generation ability, two compounds were rationally designed with D-π-A molecular skeleton, in which phenyl and furan ring was used as π-conjugation bridge for **TPCPY** and **TFCPY**, respectively (Scheme 1). Considering rich electron characteristics and twisted structure, the triphenylamine (TPA) group served as the electron donor (D) and molecular rotor. Cationic methylpyridinium with cyano moiety acted as the electron acceptor (A). The D and A units were integrated by different π-bridge to construct D-π-A-type molecules. The designed photosensitizers **TPCPY** and **TFCPY** were prepared simply through the synthetic route outlined in Scheme S1 (Supporting information). The electron-donating TPA and π-bridge were connected by the Suzuki-Miyaura coupling reaction. Then, the intermediates **TP-CHO** and **TF-CHO** were reacted with pyridylacetonitrile hydrochloride through a Knoevenagel condensation reaction. Detailed synthesis and characterization (Figs. S1–S12 in Supporting information) data are found in Supporting information.

The photophysical properties of **TPCPY** and **TFCPY** were analyzed by ultraviolet–visible (UV–vis) absorption spectra. As presented in Fig. 1A, both compounds showed typical intramolecular charge transfer (ICT) absorption profiles in dimethylsulfoxide (DMSO) solutions with broad bands from 400 nm to 700 nm. With electron-rich heterocyclic furan in the molecular skeleton, the maximal absorption wavelength of **TFCPY** (544 nm) featured a remarkable bathochromic shift with an absorption tail toward the near-infrared region in comparison with **TPCPY** (470 nm). The ICT character was further confirmed by solvatochromic effect (Fig. S13 in Supporting information). Noteworthy, the maximum molar absorption coefficient of **TFCPY** (3.07×10^5 L mol^{-1} cm^{-1}) is much higher than that of **TPCPY** (1.78×10^5 L mol^{-1} cm^{-1}), being favorable for capturing more excitation light [37,38]. To investigate the emission properties in aggregate, the PL spectra of **TPCPY** and **TFCPY** were recorded in a DMSO/toluene mixture. As illustrated in Fig. 1B and Fig. S14 (Supporting information), upon enhancing toluene fractions (f_T), the emission intensities were significantly increased due to the formation of aggregate. The PL intensity increase of **TPCPY** and **TFCPY** at 95% of toluene contents was about 15- and 17-fold higher than those in their pure DMSO solutions (Fig. 1C). As a consequence, both **TPCPY** and **TFCPY** exhibited good AIE characteristics. Both compounds displayed obvious hypochromic shift with increasing toluene fraction, which can be assigned to the solvatochromic effect of typical PSs with ICT characteristics [39-42]. The maximum emission of **TPCPY** and **TFCPY** aggregates are at 724 and 725 nm with the fluorescence quantum yields (Φ_F) of 1.2% and 1.1%, and their lifetimes are 2.04 and 2.57 ns, respectively (Fig. S15 in Supporting information). Meanwhile, **TFCPY** shown obvious emission signal in cell culture media DMEM solution compared with that of **TPCPY** (Fig. S16 in Supporting information). In addition, **TPCPY** and **TFCPY** exhibited excellent photostability (Fig. S17 in Supporting information). The specific photophysical data are summarized in Table S1 (Supporting information).

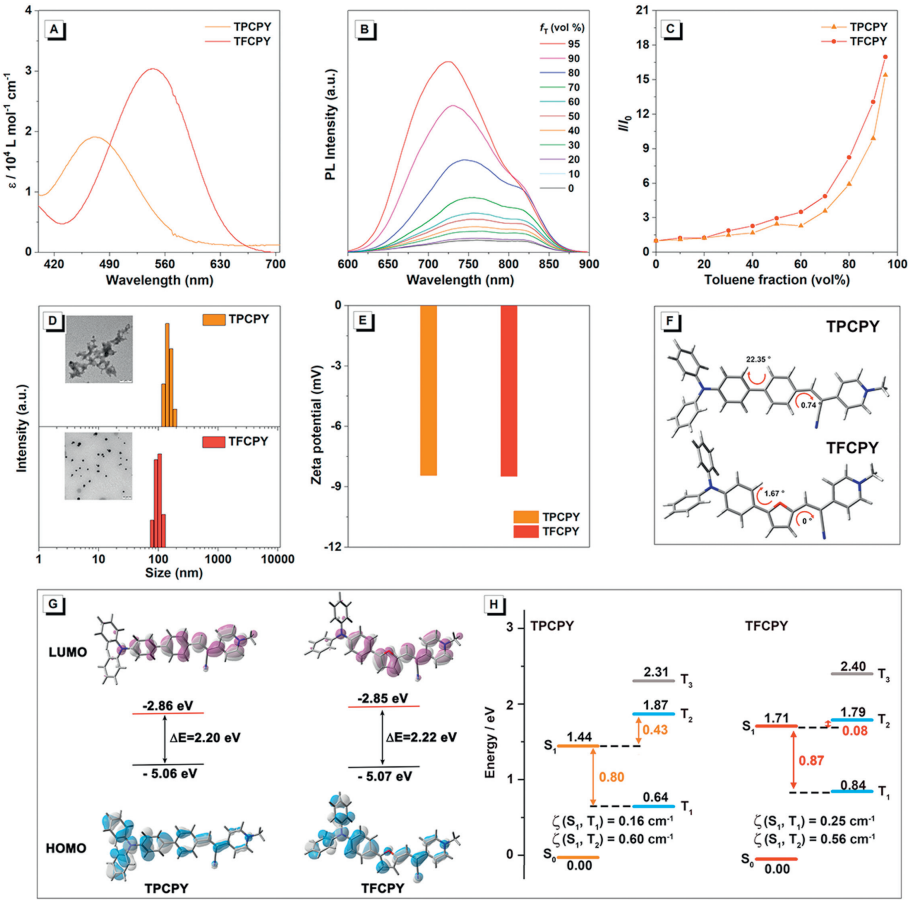

Fig. 1. (A) The absorption spectra of **TPCPY** and **TFCPY** in DMSO solutions (10 μmol/L). (B) Photoluminescence (PL) spectra of **TFCPY** (5×10^{-5} mol/L) in DMSO/toluene mixtures with different toluene fractions (λ_{ex}: 510 nm). (C) Plots of relative PL intensity (I/I_0) *versus* the composition of different solution mixtures of designed PSs. (D) The particle size distribution of both PSs detected from DLS (Insert: TEM images, scale bar: 200 nm). (E) Zeta potential of **TPCPY** and **TFCPY**. (F) Optimized molecular structures, (G) HOMO-LUMO distribution, and (H) energy level diagrams and SOC values of excited singlet and triplet states for **TPCPY** and **TFCPY** (isocontour value = 0.2).

Dynamic light scattering (DLS) analysis confirmed the formation of nanoaggregates of 2 μmol/L **TPCPY** and **TFCPY** in a DMSO/H_2O (v:v, 1:99) mixture with an average diameter of 141.8 and 105.7 nm, respectively (Fig. 1D). The transmission electron microscopy (TEM) images inserted in Fig. 1D showed different morphologies of nanoaggregates, indicating that different π-bridge can have an important influence on the aggregation behavior. All compounds in aggregate state possessed the negatively charged surface with a zeta potential of −8.43 and −8.48 mV for **TPCPY** and **TFCPY**, respectively (Fig. 1E).

Furthermore, the theoretical calculations were conducted to better understand the molecular configurations and electronic properties of **TPCPY** and **TFCPY**. As shown in Fig. 1F, the electron-withdrawing unit and π-conjugation bridge in these two compounds exhibit relatively coplanar configurations with small dihedral angles (<1°). The electron-donating unit is highly twisted structure, which is advantageous for achieving AIE nature. Incorporating furan unit as a π-bridge, **TFCPY** exhibited a V-shaped structure instead of the linear structure of **TPCPY**. As shown in Fig. 1G, both compounds possess similar electron cloud distribution. The highest occupied molecular orbitals (HOMOs) distributions were mostly on the whole molecules, whereas the lowest unoccupied molecular orbitals (LUMOs) mainly located on the electron-withdrawing part and π-bridge unit and slightly delocalized on the electron-donating groups. The results indicate that both compounds have an efficient ICT effect. The energy difference (ΔE_{ST}) and spin-orbital coupling (SOC) are primary factors in determining the ISC efficiency, further impacting ROS generation efficacy [43]. The ΔE_{ST} between the S_1 and T_1 of **TPCPY** and **TFCPY** are calculated to be 0.80 and 0.87 eV, respectively (Fig. 1H). The large energy gaps result in low ISC, which is confirmed by the calculated low SOC constant (ξ) of 0.16 and 0.25 cm^{-1} for **TPCPY** and **TFCPY**. Although similar ξ for **TPCPY** (0.60 cm^{-1}) and **TFCPY** (0.56 cm^{-1}), the energy gap between S_1 and T_2 was determined to be 0.08 eV for **TFCPY**, which is smaller than that of **TPCPY** (0.43 eV). Thus, an efficient ISC process could occur from S_1 to T_2, which endows **TFCPY** with better photosensitization functionality than **TPCPY**.

To evaluate the impact of π-bridge on PDT performance, the overall ROS production capability of **TPCPY** and **TFCPY** were investigated with classic indicator dichlorofluorescein (DCFH). DCFH alone is nearly nonfluorescent and would be activated by any type of ROS to increase its emission intensity. As illustrated in Fig. 2A and Fig. S18 (Supporting information), the emission intensity of DCFH solution coupled with **TPCPY** or **TFCPY** increased rapidly with the irradiation time prolonged, compared with the DCFH solution without any photosensitizers, demonstrating excellent ROS generation of both compounds post-irradiation. In comparison, efficient and fast ROS production was achieved by **TFCPY**, which surpassed **TPCPY** and clinical PSs including Ce6 and RB. The obtained results suggested that introducing furan ring into **TFCPY** can exhibit superior capability for ROS generation, which is in accordance with smaller ΔE_{ST} of **TFCPY** and moderate SOC value, both leading to better ISC efficiency.

To further explore the ROS species generated by **TPCPY** and **TFCPY**, an indicator of 9,10-anthracene-bis(methylene)dimalonic

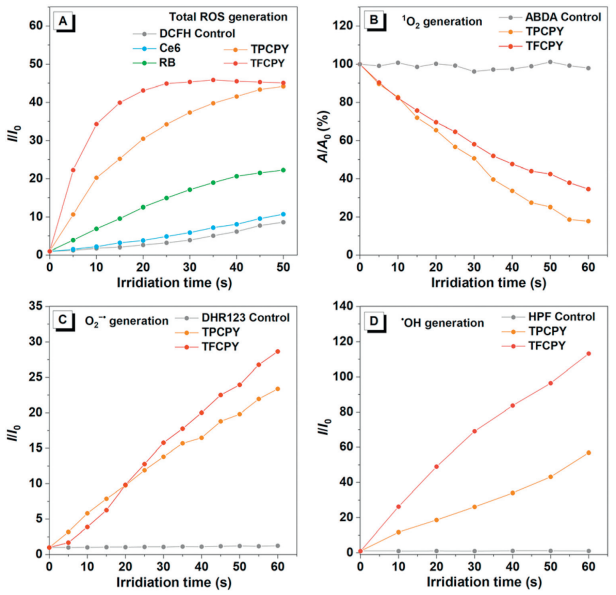

Fig. 2. ROS generation capability of **TPCPY** or **TFCPY** evaluated by different indicators under irradiation (white light, 42 mW/cm^2). (A) The relative fluorescence intensity (I/I_0) of DCFH solution at 524 nm containing PSs *versus* the irradiation time (DCFH: 40 μmol/L, photosensitizers: 2 μmol/L). (B) The decomposition rates of ABDA at 378 nm absorbance in the presence of PSs (ABDA: 100 μmol/L, photosensitizers: 20 μmol/L). (C) Time-course plots activation rates of DHR123 solution containing PSs with different irradiation time (DHR123: 5 μmol/L, photosensitizers: 2 μmol/L). (D) The relative fluorescence intensity (I/I_0) of HPF solution containing PSs *versus* the irradiation time (HPF: 5 μmol/L, PSs: 2 μmol/L).

acid (ABDA) was utilized to verify the formation of $^1O_2$. As shown in Fig. 2B and Fig. S19 (Supporting information), the ABDA solutions exhibited a sharp reduction of absorption signal in the system containing **TPCPY** or **TFCPY** upon light irradiation. The 82% and 65% of ABDA were consumed by **TPCPY** and **TFCPY** as the irradiation time extended to 60 s, indicating that **TPCPY** produced $^1O_2$ more efficiently than **TFCPY**. Moreover, dihydrorhodamine 123 (DHR123) and hydroxyphenyl fluorescein (HPF) were employed to determine the effectiveness of $O_2^{\bullet-}$ and $^{\bullet}OH$ production, respectively. As shown in Fig. 2C and Fig. S20 (Supporting information), both **TPCPY** and **TFCPY** expressed apparent enhancement of 23-fold and 28-fold in emission with extended irradiation exposure time, respectively. In addition, with the auxiliary effect of vitamin C, a widely used radical scavenger, the DHR123 fluorescence increment was quenched, further validating free radical-dominated ROS generation ability. Similar detection results were obtained for HPF (Fig. 2D and Fig. S21 in Supporting information). The gradual increase in the characteristic emission of HPF with prolonged irradiation was detected for both compounds. After 60 s irradiation, the fluorescence intensity of HPF reached 56- and 113-fold for **TPCPY** and **TFCPY**, respectively, while more significant enhancement could be discovered in **TFCPY**. All these results demonstrated that two PSs can effectively generate type I/II ROS, while the production efficiency of type I ROS was found to be higher in **TFCPY** compared to **TPCPY**, owing to the strategic incorporation of electron-rich furan ring [44,45].

Considering the remarkable type I/II ROS production and NIR emission properties of **TPCPY** and **TFCPY**, their antitumor efficacy was examined *in vitro*. As the important factor for FLI-guided PDT performance, the cell uptake capability of both compounds was first assessed by confocal laser scanning microscopy (CLSM) with HeLa cells. The HeLa cells were incubated with both compounds for different concentrations and periods. As displayed in Fig. S22 (Supporting information), the apparent fluorescence signal was observed in cells after incubation with a 0.5 μmol/L concentration of **TFCPY**, then a gradual increase with various **TFCPY** concentrations ranging from 0 to 5 μmol/L, demonstrating excellent cell penetration and fluorescence imaging ability. As shown in Fig. S23 (Supporting information), the fluorescence intensity was enhanced by prolonging the incubation time. After 30 min, the red fluorescence reached its maximum intensity, indicating that **TFCPY** could be rapidly incubated by HeLa cells. By contrast, CLSM images revealed that negligible fluorescence signals can be detectable in HeLa cells after incubating with **TPCPY** in the internalization experiment. These results are probably due to various molecular packing arrangements influenced by different π-bridge. Next, the mitochondrial-targeting behavior of **TFCPY** was studied by colocalization experiment. The images of HeLa cells in Fig. S24 (Supporting information) demonstrated that **TFCPY** can efficiently target mitochondria, as its emission signals overlapped with that of Mitotracker Green probes (Pearson correlation coefficient: 0.94). The subcellular distribution of **TFCPY** could boost its cytotoxicity in PDT.

Based on efficient cellular internalization and mitochondrial-accumulating, the intracellular ROS generation of both compounds was characterized in HeLa cells using DCFH-DA assay. As illustrated in Fig. 3A, bright green fluorescence was detected in cells treated with **TFCPY** and DCFH-DA after irradiation, while cells cultured with **TPCPY** and DCFH-DA exhibited no significant fluorescence at the same experiment condition. The obtained results indicated that **TFCPY** was able to trigger intracellular ROS generation under light irradiation. Subsequently, phototoxicities of **TPCPY** and **TFCPY** were further verified *via* standard cell counting kit-8 (CCK8) assay. As the results shown in Figs. 3B and C, **TPCPY** exhibited negligible cytotoxicity at different concentrations with or without white light irradiation. In sharp contrast, the cell killing effect was positively correlated with the concentration of **TFCPY**. After white light irradiation, **TFCPY** induced death to over 70% of HeLa cells at the concentration of 5 μmol/L, indicating a good photodynamic killing effect on cancer cells. In addition, the survival rate of HeLa cells in dark was 89%, indicative of dark cytotoxicities to some degree. Additionally, to visualize the PDT efficacy of **TPCPY** and **TFCPY**, fluorescein diacetate (FDA) and propidium iodide (PI) were employed to monitor live and dead cells, respectively. As illustrated in Figs. 3D and E, red fluorescence from PI could be observed in the cells treated by both **TFCPY** and light irradiation, while the green fluorescence almost vanished, indicating the exceptional tumoricaidal efficacy *in vitro*. However, only a green fluorescence signal can be observed in cells treated with **TPCPY**. The FDA/PI co-staining results are consistent with the ROS generation ability in HeLa cells.

Since **TFCPY** exhibited excellent performance on cellular imaging and ablation, the *in vivo* FLI-guided PDT antitumor effect was further verified by the mouse model bearing the 4T1 tumor. All the animal experiments were performed according to the guidelines of ethical review of animal welfare, and supervised by Changchun Institute of Applied Chemistry, CAS, China (IACUC Issue No. CIAC 2023. 0174). To check the imaging performance and appropriate incubation time, the fluorescence imaging experiments were carried out at different time points after intratumor injection. As illustrated in Fig. 4B, time-dependent increments in fluorescence intensity in tumor regions were observed, which could be assigned to the gradual diffusion and penetration of **TFCPY**. At 4 h postinjection, the emission signal reached the maximum level, and the tumor sections could be distinctly distinguished from surrounding tissues, laying the foundation for FLI-guided PDT. Moreover, the fluorescence emission kept intense with 12 h. Furthermore, the therapeutic capability of **TFCPY** *in vivo* on mice with the 4T1 tumor was investigated. The four groups of mice ($n = 4$) underwent the corresponding treatment as follow: (i) phosphate buffered saline (PBS), (ii) PBS with light irradiation, (iii) **TFCPY**

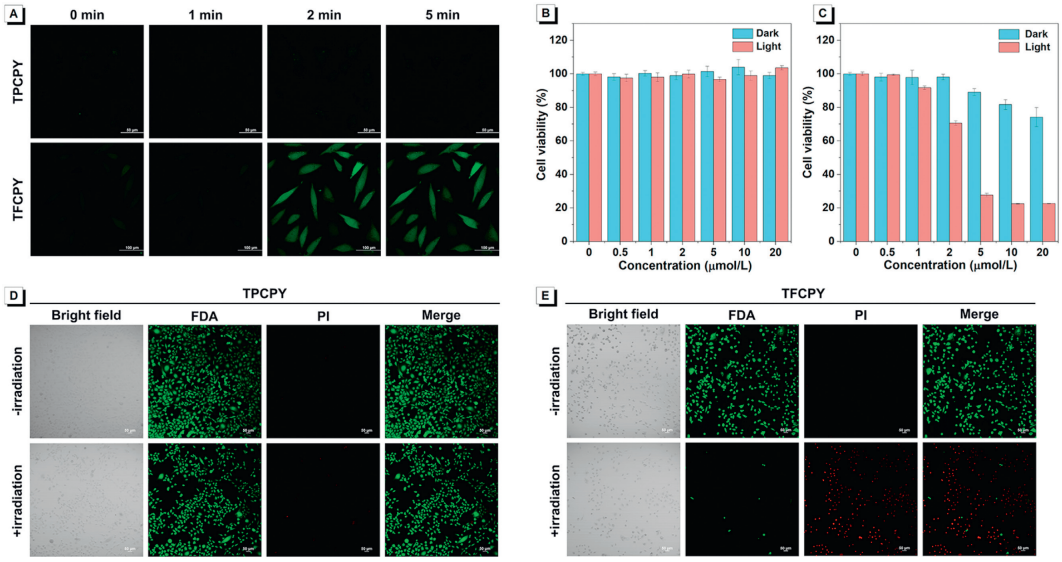

Fig. 3. (A) Intracellular ROS detection by DCFH-DA in HeLa cells treated with **TPCPY** and **TFCPY** under white light irradiation. Scale bar: 50 μm (top) and 100 μm (bottom). (B) Dose-dependent cytotoxicity of **TPCPY** to HeLa cells. (C) Dose-dependent cytotoxicity of **TFCPY** to HeLa cells. Data are presented as mean ± standard deviation (SD) ($n = 3$). (D) Live/dead cells imaging of HeLa cells stained with FDA/PI after incubation with **TFCPY** under white light irradiation. Scale bar: 50 μm. (E) Live/dead cells imaging of HeLa cells stained with FDA/PI (FDA: 1 mg/mL, PI: 100 mg/mL) after incubation with **TFCPY** under white light irradiation for 20 min (42 mW/cm^2). Scale bar: 50 μm.

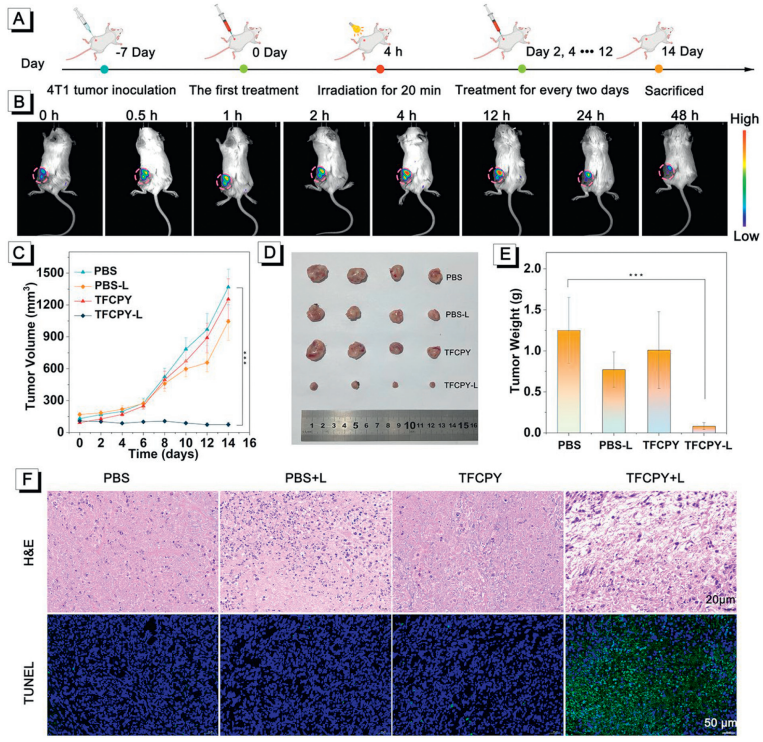

Fig. 4. *In vivo* antitumor capacity of **TFCPY** in 4T1 tumor-bearing mice model. (A) Schematic diagram of establishing tumor models and *in vivo* therapeutic process. (B) The fluorescence imaging after intratumor injection of **TFCPY** with 48 h. (C) The tumor growth curves of different treatment groups. (D) Photograph of tumor sections collected from different treatment groups. (E) The tumor tissue weights from the sacrificed mice. Data are presented as mean ± SD ($n = 4$). $^{***}P < 0.001$. (F) H&E and TUNEL staining of tumor tissues with different treatments (light treatment conditions (+L): irradiation by white light, 100 mW/cm^2).

group, (iv) **TFCPY** with light irradiation. The detailed phototherapy process was illustrated in Fig. 4A. The white light irradiation was conducted for PDT at 4 h on the basis of *in vivo* fluorescence imaging results. The volumes of the tumors in the four groups were recorded every two days to evaluate the therapeutic outcomes. The tumor growth curves demonstrated that the tumors in the control group i-iii manifested rapid and sustained growth with no significant inhibition, which demonstrated that neither the **TFCPY** nor white light irradiation could kill the tumor cells (Fig. 4C). In sharp contrast, **TFCPY** under white light irradiation notably inhibited the tumor volume throughout the entire treatment period. The representative mice photographs (Fig. S25 in Supporting information), extracted tumor images (Fig. 4D), and the mean weight of tumor tissue (Fig. 4E) further intuitively confirmed the excellent PDT tumor-inhibition efficacy of **TFCPY** under light irradiation. As shown in Fig. S26 (Supporting information), no obvious differences in body weights were found in all groups during the entire treatment process, indicating low systemic toxicity of **TFCPY**. In addi-

tion, hematoxylin and eosin (H&E) staining and immunofluorescence staining of tumor sections of each group were performed to assess the therapeutic effect *in vivo*. Significant morphological damage was observed in H&E images of the group treated with the **TFCPY** and white light irradiation, indicating severe tumor necrosis (Fig. 4F). The results from terminal deoxynucleotidyl transferase dUTP nick endlabeling (TUNEL) staining displayed obvious green fluorescence signals in tumor sections from **TFCPY**-treated group, suggesting significant cell death resulting from **TFCPY-**based PDT. Consequently, all these results strongly verified that **TFCPY** exhibited superior fluorescence imaging and therapeutic efficacy, making it competent for cancer phototheranostics.

In this work, to achieve enhancement of FLI-guided PDT efficacy, two novel D-π-A-structured of **TPCPY** and **TFCPY** have been constructed by integration of phenyl and furan ring as a π-bridge, respectively. Both compounds exhibit AIE properties and highly efficient generation of type-I and type-II ROS upon irradiation. The electron-rich furan ring introduced into **TFCPY** has proved to bring both a smaller energy gap (0.08 eV) and moderate SOC value (0.56 cm^{-1}) between S_1 and T_2, which is favorable for more efficient ISC process and ROS generation. Therefore, compared with **TPCPY**, **TFCPY** exhibits higher ROS generation and more efficient PDT killing outcomes against cancer cells under white-light irradiation. In addition, **TFCPY** possesses mitochondria targeting capability. Moreover, *in vivo* experiments indicated that **TFCPY** can achieve visualization of tumor sites and in the meantime can effectively eliminate tumors in a PDT manner. All these results indicate the excellent FLI-guided PDT efficacy of **TFCPY** in inhibiting tumor growth and imply that our design of incorporation of furan π bridge into molecular structure could enhance ROS generation and PDT efficacy.

Declaration of competing interest

The authors declare that they have no known competing financial interests or personal relationships that could have appeared to influence the work reported in this paper.

CRediT authorship contribution statement

Tong-Tong Zhou: Writing – original draft, Data curation. **Guan-Yu Ding:** Investigation, Formal analysis, Data curation. **Xue Li:** Visualization, Validation. **Li-Li Wen:** Writing – review & editing, Funding acquisition. **Xiao-Xu Pang:** Formal analysis. **Ying-Chen Duan:** Methodology. **Ju-Yang He:** Validation. **Guo-Gang Shan:** Writing – review & editing, Funding acquisition. **Zhong-Min Su:** Writing – review & editing.

Acknowledgments

This work was supported by the funding from Natural Science Foundation of Jilin Province (No. 20220101191JC), National Natural Science Foundation of China (No. 22175033), and the 13th Five-Year Program for Science and Technology of Education Department of Jilin Province (No. JJKH20230800KJ).

Supplementary materials

Supplementary material associated with this article can be found, in the online version, at doi:10.1016/j.cclet.2024.110341.

References

[1] C. Holohan, S. Van Schaeybroeck, D.B. Longley, P.G. Johnston, Nat. Rev. Cancer 13 (2013) 714–726.
[2] F. Bray, J. Ferlay, I. Soerjomataram, et al., Cancer J. Clin. 68 (2018) 394–424.
[3] X. Yang, X. Zhang, Z. Yang, et al., ACS Appl. Mater. Interfaces 16 (2024) 9816–9825.
[4] H. Zhao, N. Li, C. Ma, et al., Chin. Chem. Lett. 34 (2023) 107699.
[5] T.C. Pham, V.N. Nguyen, Y. Choi, S. Lee, J. Yoon, Chem. Rev. 121 (2021) 13454–13619.
[6] X. Zhao, J. Liu, J. Fan, H. Chao, X. Peng, Chem. Soc. Rev. 50 (2021) 4185–4219.
[7] A. Sharma, P. Verwilst, M. Li, et al., Chem. Rev. 124 (2024) 2699–2804.
[8] J. Qi, H. Ou, Q. Liu, D. Ding, Aggregate 2 (2021) 95–113.
[9] J.P. Celli, B.Q. Spring, I. Rizvi, et al., Chem. Rev. 110 (2010) 2795–2838.
[10] D.E.J.G.J. Dolmans, D. Fukumura, R.K. Jain, Nat. Rev. Cancer 3 (2003) 380–387.
[11] S. Zhang, W. Yang, X. Lu, et al., Chem. Sci. 14 (2023) 7076–7085.
[12] Y.Y. Zhao, L. Zhang, Z. Chen, et al., J. Am. Chem. Soc. 143 (2021) 13980–13989.
[13] Y. Tang, Y. Li, B. Li, et al., Nat. Commun. 15 (2024) 2530.
[14] Q. Zhao, G. Qing, J. Yu, et al., Chin. Chem. Lett. 35 (2024) 108535.
[15] V.N. Nguyen, S. Qi, S. Kim, et al., J. Am. Chem. Soc. 141 (2019) 16243–16248.
[16] Y. Yu, S. Wu, L. Zhang, et al., Biomaterials 280 (2022) 121255.
[17] J. Zhang, W. Ma, H. Luo, et al., Adv. Healthcare Mater. 13 (2024) e2303175.
[18] B. Lu, Y. Huang, Z. Zhang, H. Quan, Y. Yao, Mater. Chem. Front. 6 (2022) 2968–2993.
[19] Y.Y. Zhao, H. Kim, V.N. Nguyen, et al., Coord. Chem. Rev. 501 (2024) 215560.
[20] W.F. Watson, R. Livingston, Nature 162 (1948) 452–453.
[21] Z. Zhao, H. Zhang, J.W.Y. Lam, B.Z. Tang, Angew. Chem. Int. Ed. 59 (2020) 9888–9907.
[22] Z. Li, B.Z. Tang, D. Wang, Adv. Mater. 36 (2024) 2406047.
[23] M.Y. Wu, M. Gu, J.K. Leung, et al., Small 17 (2021) e2101770.
[24] J. Wang, Y. Wang, Z. Li, et al., Chin. Chem. Lett. 35 (2024) 108934.
[25] Z. Liu, Q. Wang, W. Qiu, et al., Chem. Sci. 13 (2022) 3599–3608.
[26] P. Cen, J. Huang, C. Jin, et al., Aggregate 4 (2023) e352.
[27] H. Zhang, C. He, L. Shen, et al., Chin. Chem. Lett. 34 (2023) 108160.
[28] G. Feng, B. Liu, Small 12 (2016) 6528–6535.
[29] X. Yang, X. Wang, X. Zhang, et al., Adv. Mater. 36 (2024) 2402182.
[30] H. Xie, Z. Bi, J. Yin, et al., ACS Nano 17 (2023) 4591–4600.
[31] A.M. Smith, M.C. Mancini, S. Nie, Nat. Nanotechnol. 4 (2009) 710–711.
[32] X. Cai, B. Liu, Angew. Chem. Int. Ed. 59 (2020) 9868–9886.
[33] X. Chen, L. Shi, X.Y. Ran, et al., Adv. Funct. Mater. 34 (2024) 2400728.
[34] P. Zhang, H. Kuang, Y. Xu, et al., ACS Appl. Mater. Interfaces 12 (2020) 42551–42557.
[35] Y. Gui, Y. Wang, D. Wang, et al., Angew. Chem. Int. Ed. 63 (2024) e202318609.
[36] S. Yang, J. Zhang, Z. Zhang, et al., J. Am. Chem. Soc. 145 (2023) 22776–22787.
[37] P. Wang, S. Guo, H.J. Wang, et al., Nat. Commun. 10 (2019) 3155.
[38] S. Guo, K.K. Chen, R. Dong, et al., ACS Catal. 8 (2018) 8659–8670.
[39] H.Y. Wang, X.Y. Zheng, L.S. Long, L.S. Zheng, X.J. Kong, Tungsten 5 (2023) 254–260.
[40] M. Cao, T. Zhu, M. Zhao, et al., Anal. Chem. 94 (2022) 10676–10684.
[41] L.H. Xiong, L. Yang, J. Geng, B.Z. Tang, X. He, ACS Nano 18 (2024) 17837–17851.
[42] S. Song, Y. Zhao, M. Kang, et al., Adv. Mater. 36 (2024) e2309748.
[43] J. Wang, H. Li, Y. Zhu, et al., Chem. Sci. 14 (2023) 323–330.
[44] W. Chen, Z. Wang, G. Hong, et al., Chem. Sci. 15 (2024) 10945–10953.
[45] Y. Li, D. Zhang, Y. Yu, et al., ACS Nano 17 (2023) 16993–17003.